Aerostructural Optimization of a Transonic Compressor Rotor

Yongsheng Lian[*]
Ohio Aerospace Institute, Cleveland, Ohio, 44142
and
Meng-Sing Liou[†]
NASA John H. Glenn Research Center at Lewis Field, Cleveland, Ohio 44135

This paper presents a framework for multi-objective and multidisciplinary design optimization using high-fidelity analysis tools. In this framework the aerodynamic performance is evaluated based on a Navier–Stokes equation solver, and the structure dynamics is computed using commercially available finite element software. We employ a genetic algorithm as a robust design optimization tool to facilitate the multi-objective optimization. We also use the response surface approach to tackle the difficulties associated with the organizational complexity and computational burden inherent in the multidisciplinary optimization. The coupling between the fluid solver and structural solver is realized through a thin-plate spline interpolation algorithm. The proposed approach is then used to perform aerostructural optimization of a three-dimensional transonic compressor blade. Our numerical results show that this method can improve the existing design and reduce the required computational time by orders of magnitude.

I. Introduction

WITH the advancement of computational power and computational methods, researchers have used optimization techniques to improve the performance of complex system, such as aircraft engine. In this instance, Oyama et al. minimized the entropy generation of the NASA rotor67 blade,[1] Benini improved the total pressure ratio and the adiabatic efficiency of the NASA rotor37 blade,[2] Mengistu and Ghaly[3] performed multipoint design of different compressor rotors to improve their aerodynamic performance, and Lian and Liou[4] carried out multi-objective optimization of the NASA rotor67 blade. These analyses were focused on a single-discipline response, namely, the aerodynamic aspect. However, compressor design is inherently multidisciplinary, and a successful design should involve a combination of a variety of disciplines including aerodynamics, structure dynamics, acoustics, and control theory.[5] In addition, the present design procedures are usually based on sequential discipline optimization, which might be insufficient to provide a satisfactory result. The resulting solution might satisfy some, but not all of the requirements. In that case, the coupled multidisciplinary optimization (MDO) design technique is required.

The applications of MDO to compressor designs give rise to considerable challenges. First, the computational expense associated with MDO is usually much higher than the sum of the costs associated with each single-discipline optimization. Second, organizational complexity imposes another challenge.[6] For example, different analysis codes can run on different machines at different sites. For these two reasons, a direct coupling of an optimizer with multidisciplinary analysis tools might be practically difficult, especially when a large number of design variables and computationally intensive tools are involved. Third, noisy or jagged response from some disciplines deteriorates the coupling effect and can lead to local

optimal design solutions. Last, in our multi-objective compressor design problem, the objectives are competing.[4] Instead of having a single optimal solution, our studied problems have a set of compromised solutions (Pareto-optimal solutions) in which none of the solution is better than the other with respect to all objectives. Traditional optimization methods usually convert such a multi-objective optimization problem into a single-objective problem by introducing additional parameters that favor a specific Pareto-optimal solution. To find more Pareto-optimal solutions, we need to start over by changing the values of parameters.

The response surface technique is particularly suitable for MDO. This technique usually approximates the objective and constraint functions with low-order polynomials, which are fitted to a set of preselected design points. With the approximation models, the computational cost is greatly reduced. Moreover, because response surface technique preselects the design points, it provides a simple way to connect different codes from various disciplines.[6] Consequently, this reduces the organizational complexity and facilitates a loose coupling among different modules. When multi-objective optimization is encountered in MDO, we can facilitate the computation with evolutionary algorithms (EAs). EA's population approach can be exploited to emphasize all compromised solutions in a population equally and to preserve a diverse set of multiple compromised solutions using a niche-preserving operator.[7] As a consequence, EAs can find as many Pareto-optimal solutions as possible in one run. For these reasons we focus on integrating the response surface technique with a genetic algorithm to perform multidisciplinary and multi-objective optimization designs.

Our objectives are to maximize the compressor stage pressure ratio and to minimize the compressor weight of a transonic compressor blade under a set of real-world constraints. To faithfully represent a variety of nonlinear phenomena in the compressor blade study, such as shock waves and boundary-layer separation, which are crucial to accurately evaluate the blade aerodynamic performance, we use high-fidelity computational-fluid-dynamics (CFD) analysis tools. Early aerostructural optimization, mainly caused by the availability of computing resources, largely relies on empirical or simple one-dimensional models with a small number of design variables, which is true especially at the conceptual design level and preliminary design level. With the recent advancement in optimization methods and affordable computing power, such rudimentary models need to be improved, and high-fidelity modeling represents the trend in MDO applications. For example, Borland et al.[8] performed

*Senior Researcher, 22800 Cedar Point Road; currently Research Area Specialist at the University of Michigan, Ann Arbor, MI 48109; ylian@umich.edu. Member AIAA.
†Senior Scientist, MS 5-11. Associate Fellow AIAA.

aerostructural optimization of a high-speed civil transport using the thin Navier–Stokes equations and a finite element based structural model; Martins et al.[9] used a Reynolds-averaged Navier–Stokes code and a finite element structural solver to optimize a natural laminar-flow supersonic business jet. Giunta[10] and Maute et al.[11] also used high-fidelity models in their works. In our work we use a three-dimensional Navier–Stokes solver to analyze the aerodynamic performance of the compressor blade. A commercial software ANSYS is adopted as the computational structure dynamics (CSD) solver to perform static aeroelastic analysis. Each objective function is approximated with a computationally cheap surrogate model. A genetic algorithm is then applied on the surrogate models for a set of Pareto-optimal solutions. At last, representative solutions are chosen from the Pareto-optimal front and validated by the high-fidelity tools.

This paper is constructed as follows: 1) formulating the multi-objective and multidisciplinary problem; 2) introducing the analysis tools for the participating disciplines; 3) presenting the coupling approach between the two disciplines through an interpolation technique; 4) introducing the optimization method; and 5) performing multi-objective and multidisciplinary optimization for a transonic compressor blade.

II. Problem Formulation

The NASA rotor67 chosen for study is a low-aspect-ratio design rotor and is the first-stage rotor of a two-stage fan. The rotor design pressure ratio is 1.63 at a mass flow rate of 33.25 kg/s. The design rotational speed is 16,043 rpm, which yields a tip speed of 429 m/s and an inlet tip relative Mach number of 1.38. The rotor has 22 blades. Based on the average span and root axial chord, it has an aspect ratio of 1.56. The rotor solidity varies from 3.11 at the hub to 1.29 at the tip. The inlet and exit tip diameters are 51.4 and 48.5 cm, respectively, and the inlet and exit hub/tip radius ratios are 0.375 and 0.478, respectively. The Reynolds number based on the hub chord length and inlet flow velocity is 1.797×10^6. The rotor is made of generic titanium, which has a density of 4500 kg/m^3 and a yield limit of 7.86×10^8 Pa. Its Young's modulus is 1.16×10^{11} Pa, and Poisson's ratio is 0.32. It is noted here that all of these property values are taken in average sense.

The blade geometry is obtained by superimposing a perturbation blade on the baseline. The perturbation blade is obtained by linearly interpolating four blade profiles along the span (hub, 31% span, 62% span, and tip). Each profile is defined by a mean camber line and thickness distributions and is parameterized by a third-order B-spline curve. The thickness distribution is determined by five design variables and the camber by three design variables. Consequently, eight design variables are used to represent a blade profile, resulting in 32 design variables for the rotor-blade surface. By doing this, we can recover the baseline geometry by setting all of the design variables to zero. To make the optimization results comparable to those of the baseline configuration, we maintain the chord distribution along the span and fix the meridional contour of the hub, casing, the sweep, and lean.

The multi-objective and multidisciplinary design optimization problem can be formulated as follows:

Maximize:

$$p_{02}/p_{01}$$

Minimize:

$$W$$

Subject to:

$$S_F > 1.5$$

$$\frac{|\dot{m} - \dot{m}_0|}{\dot{m}_0} < 0.005$$

$$x_{iL} \leq x_i \leq x_{iU} \qquad i = 1, \ldots, n$$

where p_{01} is the inlet total pressure, p_{02} is the outlet total pressure, p_{02}/p_{01} is the stage pressure rise, W is the blade weight, and S_F is the safety factor. In deterministic design, the safety factor is defined as

$$S_F = R_N/S_N \tag{1}$$

where S_N and R_N are the nominal values of the von Mises stress and yield stress, respectively. The maximal von Mises stress, which is typically used design stress for complex loading condition, is defined as follows:

$$S_N = \sqrt{\frac{(\sigma_1 - \sigma_2)^2 + (\sigma_2 - \sigma_3)^2 + (\sigma_3 - \sigma_1)^2}{2}} \tag{2}$$

where σ_1, σ_2, and σ_3 are the principle stresses. $\dot{m}$ is the mass flow rate, subscript 0 represents the baseline design, x_i is the design variable that is used to parameterize the blade geometry, x_{iL} and x_{iU} are the lower and upper bounds of the design variable, respectively, and n is the number of design variables. In our problem we take the lower bound as 95% of the baseline value and the upper bound as 105% of the baseline value. In this multidisciplinary optimization problem, the aerodynamic objective is to maximize the stage pressure ratio, and the structural objective is to minimize the structural weight of the airfoil only. (The hub or bore under the airfoil is unchanged.) The aerodynamic constraint is imposed to ensure that the new design has mass flow rate comparable to the baseline design; the structural constraint is enforced so that the safety factor of the new design is higher than a threshold safety factor. In aerospace engineering design, the safety factor is set as 1.4 or 1.5.

III. Fluid Solver

A high-fidelity CFD tool, TRAF3D (Ref. 12), is used to analyze the blade performance. TRAF3D solves the following three-dimensional, unsteady, Reynolds-averaged Navier–Stokes equations for a rotating blade passage in conservative form in curvilinear coordinates,

$$\frac{\partial \mathbf{Q}}{\partial t} + \frac{\partial \mathbf{F}}{\partial \xi} + \frac{\partial \mathbf{G}}{\partial \eta} + \frac{\partial \mathbf{H}}{\partial \zeta} = \frac{\partial \mathbf{F}_v}{\partial \xi} + \frac{\partial \mathbf{G}_v}{\partial \eta} + \frac{\partial \mathbf{H}_v}{\partial \zeta} + \mathbf{S} \tag{3}$$

The conservative variable vector and fluxes are

$$\mathbf{Q} = J^{-1} \begin{Bmatrix} \rho \\ \rho u \\ \rho v \\ \rho w \\ \rho e \end{Bmatrix}, \qquad \mathbf{F} = J^{-1} \begin{Bmatrix} \rho U \\ \rho u U + \xi_x p \\ \rho v U + \xi_y p \\ \rho w U + \xi_z p \\ \rho h U + \xi_t p \end{Bmatrix}$$

$$\mathbf{G} = J^{-1} \begin{Bmatrix} \rho V \\ \rho u V + \eta_x p \\ \rho v V + \eta_y p \\ \rho w V + \eta_z p \\ \rho h V + \eta_t p \end{Bmatrix}, \qquad \mathbf{H} = J^{-1} \begin{Bmatrix} \rho W \\ \rho u W + \zeta_x p \\ \rho v W + \zeta_y p \\ \rho w W + \zeta_z p \\ \rho h W + \zeta_t p \end{Bmatrix}$$

$$\mathbf{S} = J^{-1} \begin{Bmatrix} 0 \\ 0 \\ \rho \Omega w \\ -\rho \Omega v \\ 0 \end{Bmatrix} \tag{4}$$

where ρ, u, v, w, p, T, e, and h denote the density, velocity components in the x, y, and z directions, pressure, temperature, specific total energy, and specific total enthalpy, respectively, and Ω is the angular velocity of the rotating Cartesian system. J is the Jacobian of transformation

$$J^{-1} = x_\xi y_\eta z_\zeta + x_\eta y_\zeta z_\xi + x_\zeta y_\xi z_\eta - x_\xi y_\zeta z_\eta - x_\eta y_\xi z_\zeta - x_\zeta y_\eta z_\xi \tag{5}$$

U, V, W are the contravariant velocities,

$$U = \xi_t + \xi_x u + \xi_y v + \xi_z w, \qquad V = \eta_t + \eta_x u + \eta_y v + \eta_z w$$

$$W = \zeta_t + \zeta_x u + \zeta_y v + \zeta_z w \qquad (6)$$

and the transformation metrics are defined by

$$\xi_x = J(y_\eta z_\zeta - y_\zeta z_\eta), \qquad \xi_y = J(z_\eta x_\zeta - z_\zeta x_\eta)$$

$$\xi_z = J(x_\eta y_\zeta - x_\zeta y_\eta)$$

$$\eta_x = J(y_\zeta z_\xi - y_\xi z_\zeta), \qquad \eta_y = J(z_\zeta x_\xi - z_\xi x_\zeta)$$

$$\eta_z = J(x_\zeta y_\xi - x_\xi y_\zeta) \qquad (7)$$

$$\zeta_x = J(y_\xi z_\eta - y_\eta z_\xi), \qquad \zeta_y = J(z_\xi x_\eta - z_\eta x_\xi)$$

$$\zeta_z = J(x_\xi y_\eta - x_\eta y_\xi)$$

$$\xi_t = x_t \xi_x + y_t \xi_y + z_t \xi_z, \qquad \eta_t = x_t \eta_x + y_t \eta_y + z_t \eta_z$$

$$\zeta_t = x_t \zeta_x + y_t \zeta_y + z_t \zeta_z$$

$$x_t = 0, \qquad y_t = -\Omega z, \qquad z_t = \Omega y \qquad (8)$$

The viscous term are written as

$$\boldsymbol{F}_v = J^{-1} \begin{Bmatrix} 0 \\ \xi_x \tau_{xx} + \xi_y \tau_{xy} + \xi_z \tau_{xz} \\ \xi_x \tau_{yx} + \xi_y \tau_{yy} + \xi_z \tau_{yz} \\ \xi_x \tau_{zx} + \xi_y \tau_{zy} + \xi_z \tau_{zz} \\ \xi_x \beta_x + \xi_y \beta_y + \xi_z \beta_z \end{Bmatrix}$$

$$\boldsymbol{G}_v = J^{-1} \begin{Bmatrix} 0 \\ \eta_x \tau_{xx} + \eta_y \tau_{xy} + \eta_z \tau_{xz} \\ \eta_x \tau_{yx} + \eta_y \tau_{yy} + \eta_z \tau_{yz} \\ \eta_x \tau_{zx} + \eta_y \tau_{zy} + \eta_z \tau_{zz} \\ \eta_x \beta_x + \eta_y \beta_y + \eta_z \beta_z \end{Bmatrix}$$

$$\boldsymbol{H}_v = J^{-1} \begin{Bmatrix} 0 \\ \zeta_x \tau_{xx} + \zeta_y \tau_{xy} + \zeta_z \tau_{xz} \\ \zeta_x \tau_{yx} + \zeta_y \tau_{yy} + \zeta_z \tau_{yz} \\ \zeta_x \tau_{zx} + \zeta_y \tau_{zy} + \zeta_z \tau_{zz} \\ \zeta_x \beta_x + \zeta_y \beta_y + \zeta_z \beta_z \end{Bmatrix} \qquad (9)$$

where

$$\tau_{xx} = 2\mu u_x + \lambda(u_x + v_y + w_z), \quad \tau_{yy} = 2\mu v_y + \lambda(u_x + v_y + w_z)$$

$$\tau_{zz} = 2\mu w_z + \lambda(u_x + v_y + w_z), \qquad \tau_{xy} = \tau_{yx} = \mu(u_y + v_x)$$

$$\tau_{xz} = \tau_{zx} = \mu(u_z + w_x), \qquad \tau_{yz} = \tau_{zy} = \mu(v_z + w_y)$$

$$\beta_x = u\tau_{xx} + v\tau_{xy} + w\tau_{xz} + kT_x$$

$$\beta_y = u\tau_{yx} + v\tau_{yy} + w\tau_{yz} + kT_y$$

$$\beta_z = u\tau_{zx} + v\tau_{zy} + w\tau_{zz} + kT_z \qquad (10)$$

Based on the Stokes hypothesis, λ is taken to be $-\frac{2}{3}\mu$. The pressure is obtained based on the equation of state. The molecular coefficient of viscosity μ is determined as a function of temperature by the Sutherland's law. The space discretization uses a second-order central difference scheme with eigenvalue scaling used to weigh the artificial dissipation terms. The system of equations is advanced in time using an explicit four-stage Runge–Kutta scheme. The two-layer eddy-viscosity model of Baldwin and Lomax is used as the turbulence closure. The molecular viscosity μ and the molecular thermal conductivity k are replaced with,

$$\mu = \mu_l + \mu_t \qquad (11)$$
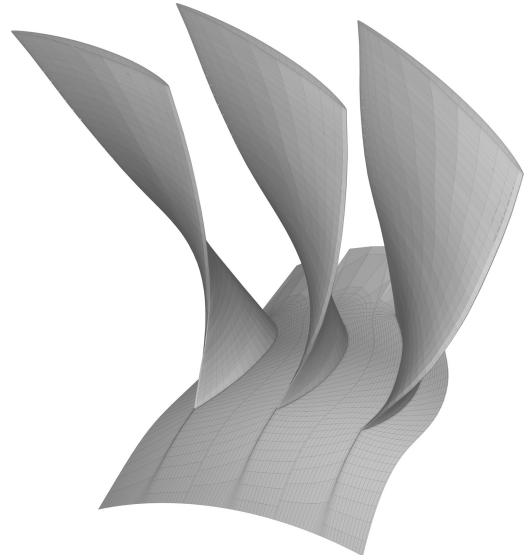
$$k = c_p[(\mu/Pr)l + (\mu/Pr)t] \qquad (12)$$

Fig. 1   Structured grid for single passage with 0.6×10^6 nodes.

where c_p is the specific heat at constant pressure, Pr is the Prandtl number, and the subscripts l and t represent laminar and turbulent, respectively.

For a single passage, the chordwise, tangential, and spanwise grid point numbers are 201, 53, and 57, respectively. This leads to 0.6×10^6 nodes per single passage. The structured CFD grid is shown in Fig. 1. We assume periodicity in the flow over a single blade passage and only need to compute one passage. At the inlet, the flow angles, total pressure, and total temperature are specified, while the outgoing Riemann invariant is taken from the interior according to the theory of characteristics. At the subsonic-axial outlet, the average value of the static pressure at the hub is prescribed, and the density and velocity components are extrapolated together with the circumferential distribution of pressure. On the solid wall we apply a constant temperature boundary condition and extrapolate the pressure from the interior points. The no-slip boundary condition and the temperature condition are used together to compute density and total energy.[13] We set periodic phantom cell values to impose the periodic condition from blade passage to blade passage. We use phantom cells to overlap the real ones where the grid is not periodic. The values of dependent variables in the phantom cells are computed using linear interpolations. The clearance region is handled by imposing periodicity conditions across the airfoil. The capability of this code has been validated by comparing the computational results to experimental data.[12,13] For each simulation, a converged solution is assumed when the residuals of the continuity equation, momentum equations, and energy equation all have dropped by an order of four.

IV.   Finite Element Model and Structural Solver

The blade has a root chord of 9.14 cm. The blade thickness, which is about 9.5% of the root chord, is much smaller than either the chord or span dimension. We also know from the wind-tunnel test that at the operating condition the blade deflection is much smaller than the blade thickness. For these reasons, we model the blade with quadrilateral plate element, which is a commonly used element for modeling plates, shells, and membranes. This element can represent in-plate, bending, and transverse shear behavior. The element has six degrees of freedom at each node: translations in the nodal x, y, and z directions and rotations about the nodal x, y, and z axes. For each element we assume element-constant thickness and element-constant pressure. By doing this we avoid zero-thickness elements at the leading and trailing edges. The blade is structurally fixed at the hub. Therefore, the nodes at the hub are fully constrained. A grid-sensitivity test is performed, and the results are shown in Table 1. For all of the grids, the variation of mass is fairly small. The maximal displacement approaches 1.29 mm with the increase of grid size; the

Table 1 Grid-sensitivity test for CSD grid

Grid size	Weight, kg	Maximal displacement, m	Maximal shear, MPa
20×20	0.2273	$0.125E\text{--}2$	450.9
30×30	0.2285	$0.127E\text{--}2$	449.7
40×40	0.2292	$0.129E\text{--}2$	455.8
50×50	0.2296	$0.129E\text{--}2$	460.7
60×60	0.2299	$0.129E\text{--}2$	461.2
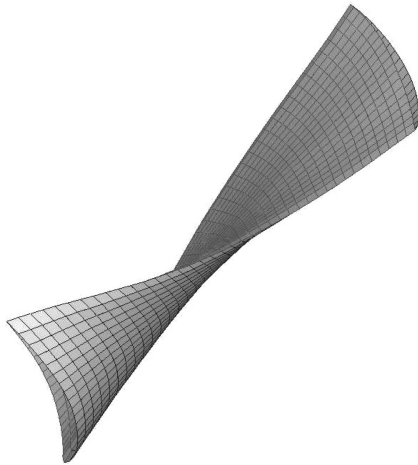
Fig. 2 Quadrilateral shell element mesh for the blade.

variation of maximal shear is less than 0.11% between grid 50×50 and grid 60×60. Based on these, we choose a grid size of 50×50 in our future test. This results in 2401 shell elements and 14,700 degrees of freedom. The CSD mesh for the blade is shown in Fig. 2.

Commercial software ANSYS is adopted as our structural solver. It solves the following structural equilibrium equation:

$$\boldsymbol{K}\boldsymbol{d} = \boldsymbol{F} \tag{13}$$

where $\boldsymbol{K}$ is the stiffness matrix, $\boldsymbol{d}$ is the displacement vector, and $\boldsymbol{F}$ is the force vector, which includes the aerodynamic pressure force and centrifugal force.

V. Aerostructural Coupling

In our MDO problem we assume that the compressor operates at its design condition and the structural response of the compressor blade is static. In addition, based on the fact from Table 1 that the structural deformation is small, we can further assume that the aerodynamic pressure distribution does not change with the structural deformation. Therefore the coupling is one way only, that is, aero-to-stress. If the blade is manufactured, the manufactured blade should deviate from the optimized blade. The reason is to use the structural deformation to offset such deviation and bring the blade to its optimized shape and therefore compensate the effects of structural deformations on aerodynamic performance. This approach is called jig-shape approach in MDO literature.[6] As a consequence, we only need to transfer the aerodynamic forces from the CFD grid to the CSD grid. This greatly simplifies our aerostructural coupling. The studied blade rotational speed does not vary much during most of the flight; it is therefore safe to consider the structural constraint under operational condition. The jig-shape approach is effective under such circumstance. For situations where flight conditions vary a lot, such as helicopter rotor blades, the jig-shape approach can only partially compensate the effects of structural deformations. More sophisticated methods should be used to consider the interaction between the aerodynamic and structural response. Interested readers are referred to the work of Friedmann,[14] Chattopadhyay and McCarthy,[15] Yuan and Friedmann,[16] Livne and Li,[17] and Walsh et al.[18]
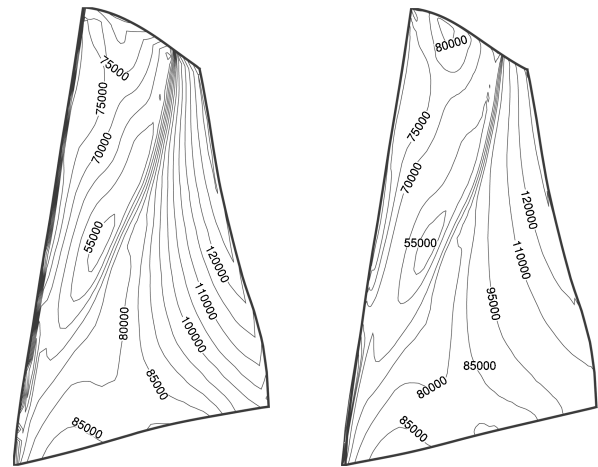
a) Pressure contours on the CSD grid

b) Pressure contours on the CFD grid

Fig. 3 Comparison of pressure contours on the CFD and CSD grids.

The CFD solver and CSD solver do not necessarily share identical grid points at the interface; therefore, interpolations are required to allow the information exchange. Smith et al.[19] evaluated suitable methods to exchange information between the CFD and CSD grids. In our problem, we need to map the aerodynamic pressure forces from the CFD grid to the CSD grid. A thin-plate spline interpolation method[20] is adopted for this purpose. The thin-plate spline interpolation is a global interpolation method, and it is invariant with respect to rotations and translations. A one-dimensional version of the interpolation is

$$P(x) = \sum_{i=1}^{N} \alpha_i |x - x_i|^2 \log |x - x_i| \tag{14}$$

where $P(x)$ is the pressure distribution function on the CSD grid, α_i is the undetermined coefficient, N is the number of monitored CFD nodes on the interface, and x_i are their locations. Once the flow equations are solved, we can transform the pressure from the CFD grid to the CSD grid:

$$P_{\text{csd}} = \boldsymbol{G} P_{\text{cfd}} \tag{15}$$

where $\boldsymbol{G}$ is the interpolation matrix derived from Eq. (14). It was pointed out by Brown that the transfer of pressure forces from the CFD grid to the CSD grid must ensure the consistency and conservation.[21] The TPS interpolation is derived based on the principle of virtual work and thus automatically guarantees the conservation of energy between the flow and the structural systems.[22] Figure 3 shows that the interpolated pressure contours on the CSD grid match well the pressure contours on the CFD grid.

VI. Optimization Method

We choose a genetic algorithm as the optimizer for our multi-objective optimization problem. Genetic algorithms have been extensively used in various areas because of their broad applicability, ease of coupling with other modules, and its global perspective. Another thrust behind their popularity is that genetic algorithms can find multiple optimal solutions in one single simulation run because of their population-based approach. This characteristic makes genetic algorithms ideal candidates for multi-objective optimization problems.

Nevertheless, a direct coupling of a genetic algorithm with multidisciplinary analysis tools is impractical for several reasons. First, genetic algorithms usually suffer slow convergence and demand a large number of calls to analysis. When computationally expensive analysis tools are used, the required computational time impinges its practical applications. This is further complicated by the multidisciplinary characteristic of the problem, which requires much

more function evaluations than the sum of the function evaluations of the single-discipline optimizations involved in the MDO. Second, the synthesis of different discipline analysis tools into a central program is difficult because the analysis tools are possibly executed on different machines at different sites. Under such circumstances, a pragmatic approach is to couple the genetic algorithm with computationally cheap surrogate models (approximation models) of the objective functions and/or constraints. The optimum of the approximate model is then validated by the full analysis, and the approximate model is thereafter updated. Depending on the problem requirement and available computational resource, this process can repeat. This so-called sequential approximate optimization is a popular approach in MDO.

Response surface technologies provide a convenient approach to tackle the aforementioned difficulties. Response surface models are usually orders of magnitude cheaper than the original problems but still provide a good approximation. Response surface models can smooth out a noisy response produced by some disciplines and provide a simple way to connect codes from various disciplines. Moreover, because the design points are preselected rather than chosen by optimization algorithms, they can be repeatedly used for designs with different objective functions and/or constraints. In this work we choose the quadratic response surface model.

The adopted optimization method was successfully used to perform multi-objective optimizations of turbopumps and transonic compressor blade.[4] Later, it was augmented with a gradient-based optimization method to enhance the convergence.[23] In short, the numerical implementation of this method has the following steps: 1) sampling the design candidates based on the statistical design of experiment, 2) evaluating the objective functions and constraints using the high-fidelity tools, 3) constructing surrogate models for the objective functions and constraints, 4) searching the Pareto-optimal solutions based on the low-fidelity surrogate models using genetic algorithm, 5) updating the Pareto-optimal with local search, and 6) choosing representative solutions from the Pareto front and validating them using the high-fidelity tools.

VII.   Numerical Results

Our problem has 32 design variables; there are 561 undetermined coefficients in the quadratic response surface approximation. With the Latin hypercube design (LHD)[24] we sample 1024 design points, which represents an 80% overdetermined design. LHD is a popular method in the design of experiment. LHD generally fills the whole design space instead of focusing on the boundaries, and therefore it provides more information within a design space and is suitable for the approximation of computer experiments that mainly have system error rather than random error. These 1024 design points are first evaluated with the TRAF3D code to find the pressure ratio and mass flow rate and to extract pressure on the blade surface. The blade weight can be readily computed by integrating the blade volume. The extracted pressure is then interpolated from the CFD grid to the CSD grid with the thin-plate spline interpolation method. We then use ANSYS to perform static structural analysis to find the maximal von Mises stress on the blade. As shown in Eq. (1), we need to build four response surfaces: two for the objective functions and two for the constraints. The accuracy of these response surface approximations is evaluated by statistical measures, including the coefficient of determination R^2, the adjusted coefficient of determination R^2_{adj}, and the percentage of root mean square error %RMSE, which is the ratio of rms error to the mean of response. Table 2 shows the test results. The value of R^2_{adj} for the pressure ratio, weight, and mass flow rate is close to one, indicating that the quadratic response surface models give accurate representations of the response functions. The approximation of the maximal stress is not as good as the other three, but it still has a R^2 value of 0.9262, which means that more than 92% of the variation around the mean can be accounted for by the quadratic approximation.

The two objectives in Eq. (1) are competing. Instead of having a single optimal solution, we expect a set of Pareto-optimal solutions. To facilitate the optimization, we choose a genetic algorithm as our optimizer. Following our previous practices[4,23] in each generation,

Table 2   Statistical measures of the quadratic response surface approximations

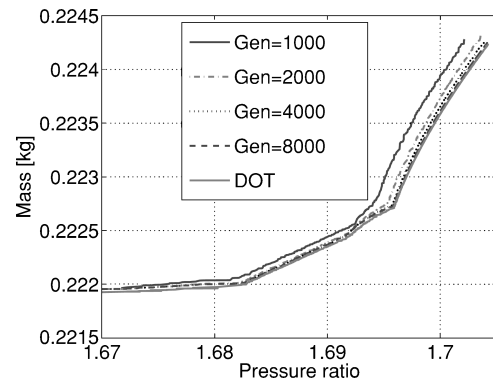| Error statistics	p_{02}/p_{01}	W	$\dot{m}$	S_N
R^2	0.9949	0.9999	0.9979	0.9262
R^2_{adj}	0.9888	0.9999	0.9954	0.8369
Mean response	1.667	0.2296 kg	33.43 kg/m^3	464.2 MPa
%RMSE	$0.3000e{-}3$	$0.1175e{-}3$	$0.1270e{-}3$	$0.2761e{-}1$

Fig. 4   Convergence analysis with different generation sizes.

we set the population size of the genetic algorithm (GA) 10 times of the number of design variables. In our case we have 32 design variables; in each generation we sample 320 individuals. Figure 4 shows the Pareto-optimal fronts in terms of generation size. The Pareto-optimal front consists of the Pareto-optimal solutions in the context of multi-objective optimization. In the context of genetic computation, we preserve every feasible solution from each generation in a pool, and each feasible solution P_i is then compared with others from the pool. If no other solution has less weight and larger pressure ratio than P_i, then P_i is a Pareto-optimal solution and belongs to the front.

The Pareto front converges with the increase of generation size. The convergence rate is fast at the beginning, but later it slows down. We are still not likely to have a converged solution after 8000 generations. The reason lies in the fact that GAs employ probabilistic operators and therefore have a slow convergence rate. A frequently used remedy is to switch to local search when the convergence rate is slow. We apply a gradient-based method after the 8000th generation. Commercially available software Design Optimization Tools (DOT)[25] is used for this purpose. In using DOT, we keep the weight as the objective function and convert the pressure ratio function as one constraint. The new problem therefore is a bounded optimization problem with three constraints. With DOT each local search begins with a point from the Pareto-optimal front at the 8000th generation. Some but not all solutions on the Pareto front can be updated, and after the local search we need to reconstruct the Pareto front. The updated Pareto-optimal front with 994 compromised solutions is shown in Fig. 4. Overall, the updated front is better than those exclusively from the genetic algorithm. Also, even though the initial condition can affect the Pareto-optimal front, these effects diminish with the increase of generation size. Different initial conditions are tested in our current study, and no evident difference exists from the initial conditions. We also perform optimization exclusively using DOT based on the response surface model. To use DOT, we convert the multi-objective problem in Eq. (1) into a single-objective problem. We use the weighted sum method to scalarize the two objective functions into one single-objective function by multiplying each objective with a weight function. This approach can give solutions better than those from the hybrid method; however, it fails to identify certain regions of the Pareto-optimal front. There are other improvements to this approach; however, they are beyond the scope of this work. For more detailed discussions in this aspect, readers are referred to the work of Deb.[7]

To verify the accuracy of our surrogate model, we validate the Pareto-optimal solutions obtained from the response surface

approximation. It will be very time consuming to verify all of those solutions. Therefore, we select 19 representative solutions using the K-means clustering technique, which chooses a subset of data to reflect the distribution of the whole data.[26] The validated results together with the baseline design are shown in Fig. 5. The verified Pareto front consists of 16 compromised solutions. Comparing with the baseline design, all the solutions increase the stage pressure ratio and reduce the weight. Some Pareto-optimal solutions increase the pressure ratio as much as 1.88% and reduce the volume by 5.36%. In Table 3 we compare characteristics between the baseline and two new designs, which represent the design with the maximal pressure ratio and design with the minimal weight. Both designs have a higher isentropic efficiency than the rotor67. The minimal weight design has larger mass flow rate, but the maximal pressure ratio design has a smaller mass flow rate than the baseline design. Also we can see from Table 3 that both designs satisfy the structural constraint.

The deformed blades of the baseline (only edges are shown) and the new design are shown in Fig. 6. Here we focus on the design with maximal pressure ratio for comparison. Compared with the new de-

Table 3   Rotor67 design performance

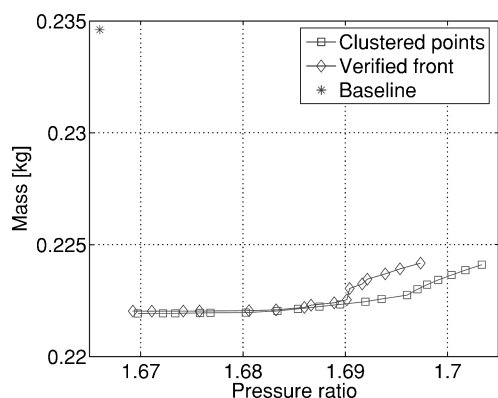| Design point	$\dot{m}$, kg/s	Isentropic efficiency	p_{02}/p_{01}	W/W_0	S_N
Minimal weight	33.716	0.9164	1.669	0.9464	1.556
Maximal pressure ratio	33.354	0.9154	1.697	0.9555	1.815
Rotor67	33.446	0.9123	1.666	1.00	1.706

Fig. 5   Pareto-front optimal solutions for the rotor67.

a) Baseline   b) Maximal pressure ratio design
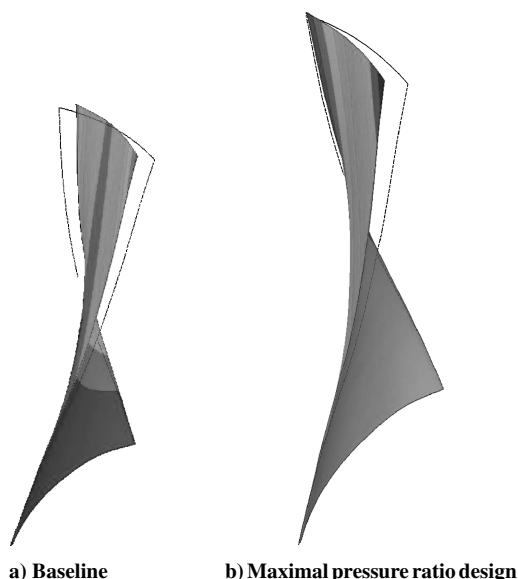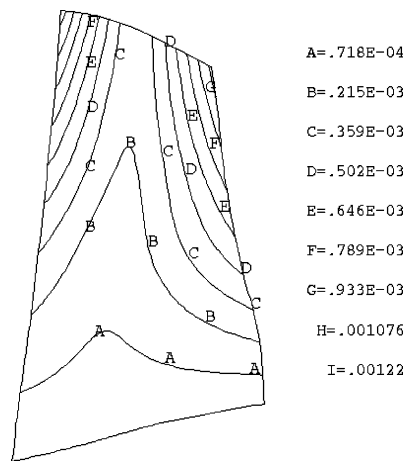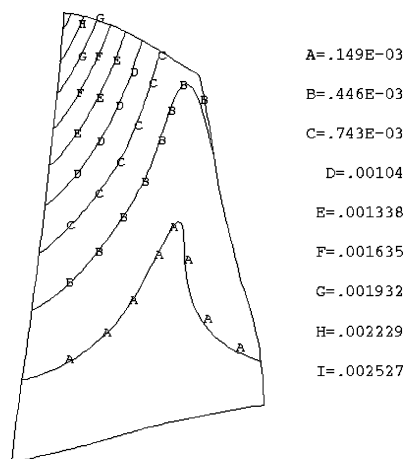
Fig. 6   Comparison of blade deformation. The edge of the undeformed blade is also shown for comparison.

a) Baseline

b) Maximal pressure ratio design

Fig. 7   Comparison of blade displacement.

sign, the baseline design has a more symmetrical deformation with respect to the middle chord. For the baseline design, the maximal deformation is 1.29 mm, which is much smaller than the blade thickness. This also confirms the justification of using the shell model. The maximal deformation occurs at the tip of the leading edge. For the maximal pressure ratio design, the maximal deformation is about 2.60 mm, which is more than twice as large as that of the baseline design and occurs at the tip of the leading edge. It is seemingly paradoxical that the new design has larger deformation but smaller maximal von Mises stress than the baseline design. The rotor blades are under both normal aerodynamic force and centrifugal force. Under such complex load, the stress is not a linear function of the strain or deformation. The deformation contours are shown in Fig. 7. The edge of the undeformed blade is also shown for comparison purpose. The maximum values shown in plots are averaged values, which differ from the reported maximum values taken at specific nodes.

To better understand the von Mises stress distribution on the new blade, we compare the stress contours on both the pressure and suction sides of the blade in Figs. 8 and 9. At the operational condition, the deformation and von Mises stress are largely caused by the centrifugal force other than caused by the aerodynamic pressure force. Even though it is not labeled in the figures, the maximal von Mises stress occurs at the blade root. We also observe that the maximal von Mises stress in the maximal pressure ratio design is about 6% less than that in the baseline. This has a collateral effect to make a safer blade design.

Two spanwise blade profiles and static-pressure coefficient are shown in Figs. 10 and 11, representing the span of 10 and 90%, respectively. At the 10% span, the high-pressure-ratio design has a larger camber but less thickness than the rotor67 design. The thinner
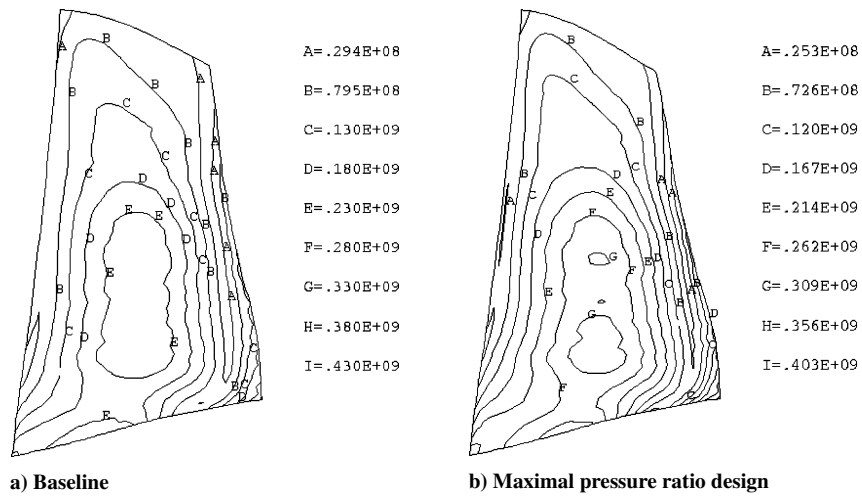
a) Baseline   b) Maximal pressure ratio design

Fig. 8   Comparison of von Mises stress on the pressure side.

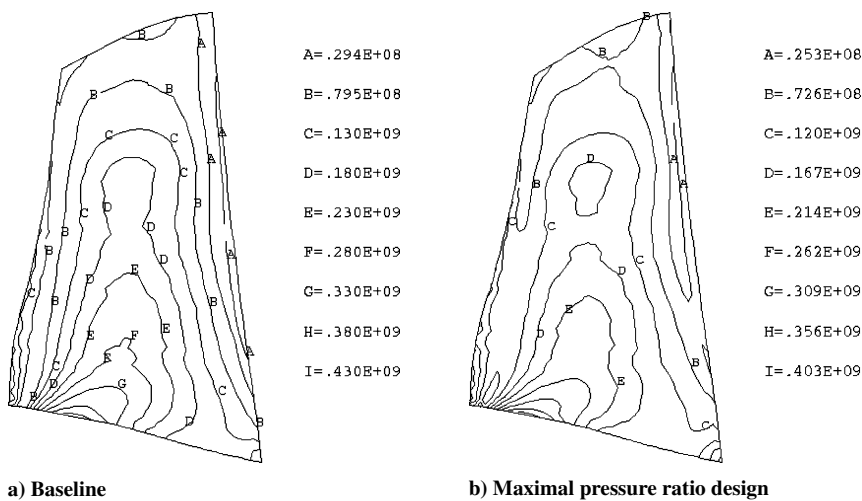a) Baseline   b) Maximal pressure ratio design

Fig. 9   Comparison of von Mises stress on the suction side.



a) Airfoil shape   b) Pressure distribution
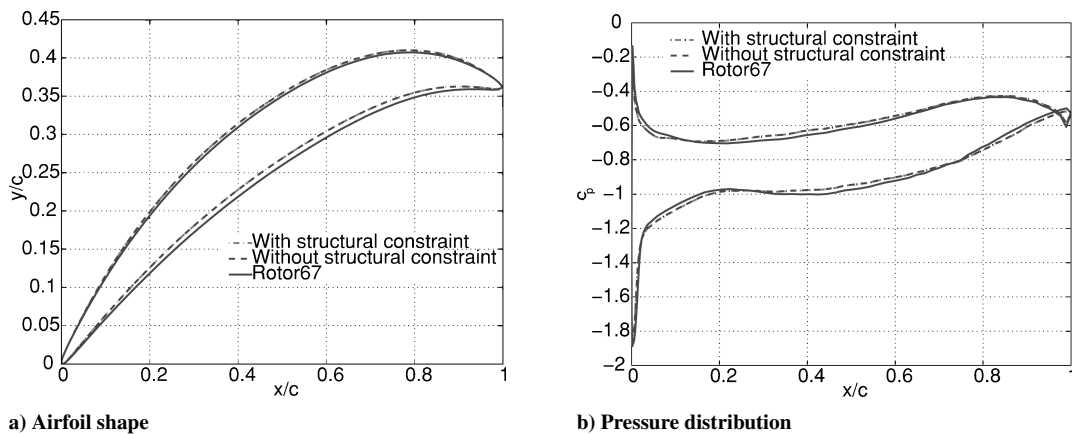
Fig. 10   Comparison between Pareto-optimal solutions and rotor67 at the 10% span from the hub.

airfoil contributes to the lighter weight of the new design. At the 90% span, the high-pressure-ratio design has a slightly smaller camber and thinner airfoil than the rotor67. Nevertheless, the pressure difference is rather large, indicating that transonic flow is sensitive to the shape change. One noticeable change is the shock position. The new design has a more forward shock wave than the rotor67. Previously we studied the same problem without considering the stress constraint.[23] Here we also compare the design without structural constraint with that with structural constraint. The difference between these two designs, in both blade profile and pressure distribution, is very small.

We use the pressure distribution on the suction side to interpret the flow pattern. Figure 12 compares the difference between the high-pressure design and the rotor67 design. Both designs have a quite strong passage shock in the upper part of the rotor. In the central part of the blade span, the passage shocks lose their intensity and become weak. The new design has a more forward shock than the rotor67 design. This observation is consistent with our finding from the pressure distribution in Fig. 11. After the shock, flow separates as a result of shock-boundary-layer interaction. This separation is evident in Fig. 13. Here, separation lines are characterized by flows going toward the line while reattachment lines look like
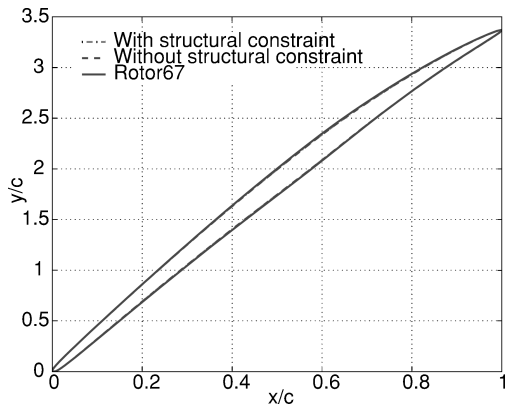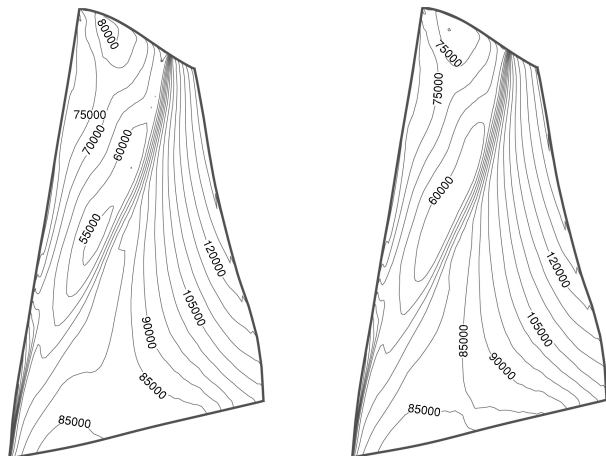
a) Airfoil shape
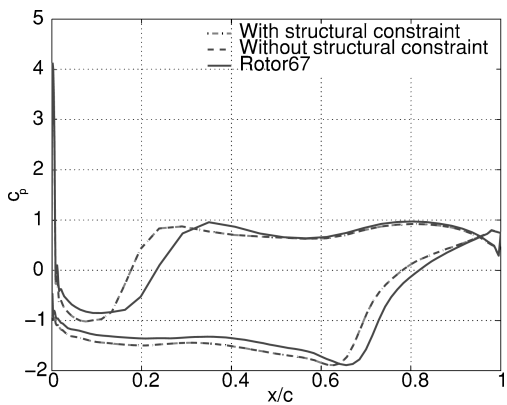
b) Pressure distribution

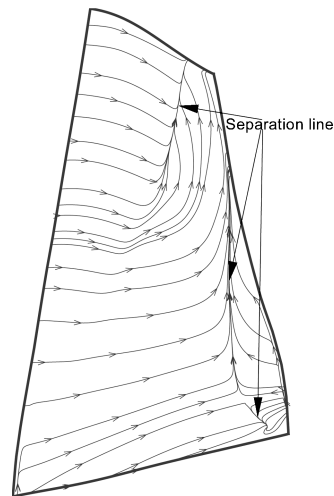Fig. 11 Comparison between Pareto-optimal solutions and rotor67 at 90% span.

a) Rotor67
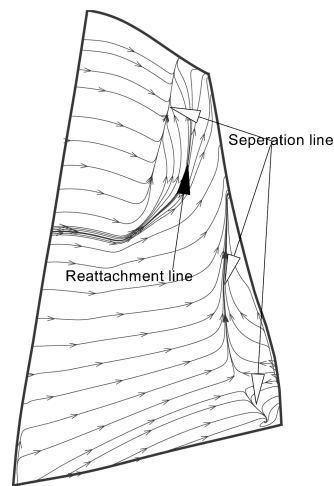
b) High-pressure-ratio design

Fig. 12 Pressure contours on the blade suction side.
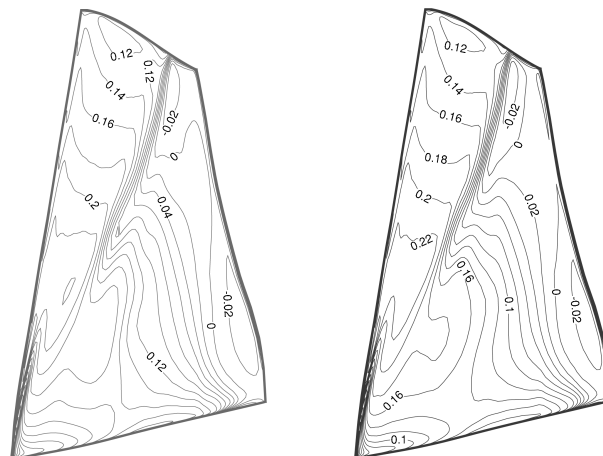

a) Rotor67

b) High-pressure-ratio design

Fig. 13 Streamlines close to the blade suction side.

a) Rotor67

b) High-pressure-ratio design

Fig. 14 Streamwise velocity contours close to the blade suction side.

flows are going away from the line. Comparing with the rotor67, the new design has a smaller separation zone after the shock, which is partially responsible for its higher stage pressure ratio. Numerical simulation shows the flow never reattaches after separation for the baseline rotor67. These separation zones are also evident in the streamwise velocity contours in Fig. 14, where the separation zone is indicated with a negative velocity.

Each CFD analysis with the TRAF3D code takes about one hour using a single Intel Intanium processor of 1.3 Ghz. With eight such processors the turnaround time to evaluate the 1024 cases is about 128 hours (5.3 days). Each structural analysis takes less than 1 min on a SGI machine with 677-MHz processor, and the total CPU time is around 10 h. Because the genetic algorithm is applied directly on the computationally cheap response surface models, the required

CPU time is less than two hours even for the 8000-generation case. The combined CPU time for the use of DOT and the construction of the response surface models and Pareto-optimal front is less than two hours. Overall we can finish the design within one week. Suppose the genetic algorithm is directly applied on the high-fidelity tools and we set the population size as 320 and generation size as 100; it will take more than five months to finish the design using the same eight processors.

We employ the quadratic response surface approximations to model the response surfaces. In general, quadratic approximations are attractive for being computationally cheap and easy to implement. However, for many nonlinear problem their modeling capability might be limited. Other approaches such as the neural network and kriging methods are proposed for nonlinear problems. It is our vision to explore those methods in our future work.

VIII. Conclusions

We presented an approach to perform multi-objective and multi-disciplinary design optimization using high-fidelity analysis tools, genetic algorithms, and response surface approximation. This effort represents our first step in developing a high-fidelity framework for multidisciplinary turbomachinery design, which is to involve fluid mechanics, structure mechanics, dynamics, heat transfer, acoustics, and control. In this work we have achieved the following: 1) using high-fidelity analysis tools to model the aerodynamic and structural characteristics of the compressor blade, 2) employing response surface technique to tackle the organizational complexity and computational burden inherent in multidisciplinary design optimization, 3) utilizing a genetic algorithm to facilitate the multi-objective optimization, 4) transferring aerodynamic load through a suitable interpolation algorithm, and 5) compensating the effect of structural deformations on aerodynamic performance with a jig-shape approach. The proposed approach was used to perform aerostructural optimization of a transonic compressor blade. We achieved an increase in the pressure ratio by 1.88% and reduction in the volume by 5.36%. The new design also satisfied both the aerodynamic and structural constraints.

Acknowledgments

References

[1]Oyama, A., Liou, M. S., and Obayashi, S., "Transonic Axial-Flow Blade Shape Optimization Using Evolutionary Algorithm and Three-Dimensional Navier–Stokes Solver," *Journal of Propulsion and Power*, Vol. 20, No. 4, 2004, pp. 612–619.

[2]Benini, E., "Three-Dimensional Multi-Objective Design Optimization of a Transonic Compressor Rotor," *Journal of Propulsion and Power*, Vol. 20, No. 3, 2004, pp. 559–565.

[3]Mengistu, T., and Ghaly, W., "Single and Multipoint Shape Optimization of Gas Turbine Blade Cascades," AIAA Paper 2004-4446, Aug.–Sept. 2004.

[4]Lian, Y., and Liou, M. S., "Multiobjective Optimization Using Coupled Response Surface Model and Evolutionary Algorithm," AIAA Paper 2004-4323, Aug.–Sept. 2004; also *AIAA Journal*, Vol. 43, No. 6, 2005, pp. 1316–1325.

[5]Chamis, C. C., "Coupled Multidisciplinary Optimization of Engine Structural Performance," *Journal of Aircraft*, Vol. 36, No. 1, 1999, pp. 190–199.

[6]Sobieszczanski-Sobieski, J., and Haftka, R. T., "Multidisplinary Aerospace Design Optimization: Survey of Recent Development," *Structural Optimiation*, Vol. 14, No. 1, 1997, pp. 1–23.

[7]Deb, K., *Multi-Objective Optimization Using Evolutionary Algorithms*, Wiley, New York, 2001.

[8]Borland, C. J., Benton, J. R., Frank, P. D., Kao, T. J., Mastro, R. A., and Barthelemy, J.-F., "Multidisciplinary Design Optimization of a Commercial Aircraft Wing-An Exploratory Study," AIAA Paper 94-4305-CP, Sept. 1994.

[9]Martins, J. R. R. A., Alonso, J. J., and Reuther, J. J., "High-Fidelity Aerostructural Design Optimization of a Supersonic Business Jet," *Journal of Aircraft*, Vol. 41, No. 3, 2004, pp. 523–530.

[10]Giunta, A. A., "A Novel Sensitivity Analysis Method for High Fidelity Multidisciplinary Optimization of Aerostructural Systems," AIAA Paper 2000-0683, Jan. 2000.

[11]Maute, K., Nikbay, M., and Farhat, C., "Coupled Analytical Sensitivity Analysis and Optimization of Three-Dimensional Nonlinear Aeroelastic Systems," *AIAA Journal*, Vol. 39, No. 11, 2001, pp. 2051–2061.

[12]Arnone, A., "Viscous Analysis of Three-Dimensional Rotor Flow Using a Multigrid Method," *Journal of Turbomachinery*, Vol. 116, No. 3, 1994, pp. 435–445.

[13]Arnone, A., Liou, M. S., and Povinelli, L. A., "Navier–Stokes Solution of Transonic Cascade Flow Using Non-Periodic C-Type Grids," *Journal of Propulsion and Power*, Vol. 8, No. 2, 1992, pp. 410–417.

[14]Friedmann, P. P., "Helicopter Vibration Reduction Using Structural Optimization with Aeroelastic/Multidisciplinary Constraints A Survey," *Journal of Aircraft*, Vol. 28, No. 1, 1991, pp. 8–21.

[15]Chattopadhyay, A., and McCarthy, T. R., "A Multidisciplinary Optimization Approach for Vibration Reduction in Helicopter Rotor Blades," *Journal of Computers and Mathematics with Applications*, Vol. 25, No. 2, 1993, pp. 59–72.

[16]Yuan, K.-A., and Friedmann, P. P., "Structural Optimization for Vibration Reduction of Composite Helicopter Rotor Blades with Advances Geometry Tips Subject to Multidisciplinary Constraints," *Proceedings of the American Helicopter Society 51st Annual Forum*, May 1995, pp. 937–956.

[17]Livne, E., and Li, W.-L., "Aeroservoelastic Aspects of Wing/Control Surface Planform Shape Optimization," *AIAA Journal*, Vol. 33, No. 2, 1995, pp. 302–311.

[18]Walsh, J. L., Young, K. C., Pritchard, J. I., Adelman, H. M., and Mantay, W. R., "Integrated Aerodynamic/Dynamic/Structural Optimization of Helicopter Rotor Blades Using Multilevel Decomposition," NASA TP-3465, ARL Technical Report 518, Jan. 1995.

[19]Smith, M. J., Hodges, D. H., and Cesnik, C. E. S., "Evaluation of Computational Algorithms Suitable for Fluid-Structure Interactions," *Journal of Aircraft*, Vol. 37, No. 2, 2000, pp. 282–294.

[20]Duchon, J. P., "Splines Minimizing Rotation-Invariant Semi-Norms in Sobolev Spaces," *Constructive Theory of Functions of Several Variables*, edited by W. Schempp and K. Zeller, Springer-Verlag, Berlin, 1977, pp. 85–100.

[21]Brown, S. A., "Displacement Extrapolation for CFD+CSM Aeroelastic Analysis," AIAA Paper 1997-1090, April 1997.

[22]Liu, F., Cai, J., Zhu, Y., Tsai, H. M., and Wong, A. S. F., "Calculation of Wing Flutter by a Coupled Fluid-Structure Method," *Journal of Aircraft*, Vol. 38, No. 2, 2001, pp. 334–342.

[23]Lian, Y., and Liou, M. S., "Multiobjective Optimization of a Transonic Compressor Rotor Using Evolutionary Algorithm," *Journal of Propulsion and Power*, Vol. 21, No. 6, 2005, pp. 979–987.

[24]Beachkofski, B., and Grandhi, R., "Improved Distributed Hypercube Sampling," AIAA Paper 2002-1274, April 2002.

[25]DOT User's Manual, ver. 4.20, Vanderplaats Research and Development, Inc., Colorado Springs, CO, 1995.

[26]Bishop, C. M., *Neural Network for Pattern Recognition*, Oxford Univ. Press, 2003, pp. 187–189.